Membrane curvature association of amphipathic helix 8 drives constitutive endocytosis of GPCRs

Jan Hendrik Schmidt[1], Rasmus Herlo[1], Joscha Rombach[1], Andreas Haahr Larsen[1], Mikkel Stoklund[1], Mathias Perslev[1], Tommas Theiss Ehlers Nielsen[1], Keenie Ayla Andersen[1], Carmen Klein Herenbrink[1], Matthew D. Lycas[1], Aske Lykke Ejdrup[1], Nikolaj Riis Christensen[1], Jan P. Christensen[2], Mootaz Salman[3], Freja Herborg[1], Ulrik Gether[1], Alexander Sebastian Hauser[4], Patricia Bassereau[5], David Perrais[6], Kenneth Lindegaard Madsen[1]

[1]Molecular Neuropharmacology and Genetics Laboratory, Department of Neuroscience, Faculty of Health and Medical Sciences; University of Copenhagen, 2200 Copenhagen N, Denmark.

[2]Department of Immunology and Microbiology, Faculty of Health and Medical Sciences; University of Copenhagen, 2200 Copenhagen N, Denmark.

[3]Department of Physiology, Anatomy and Genetics, Wolfson College, University of Oxford, Oxford OX1 3QU, UK

[4]Department of Drug Design and Pharmacology, University of Copenhagen, 2100 Copenhagen, Denmark

[5]Institut Curie, Université PSL, Sorbonne Université, CNRS UMR168, Laboratoire Physico-Chimie Curie, 75005 Paris, France

[6]Univ. Bordeaux, CNRS, Interdisciplinary Institute for Neuroscience; IINS, UMR 5297, 33000 Bordeaux, France.

Correspondance: kennethma@sund.ku.dk

One-Sentence Summary

Receptor proteins navigate cellular membranes by interacting with their curvature using an evolutionary conserved mechanism that relies on amphipathic helices and complements direct coupling to the endocytic protein machinery.

Abstract

Cellular signaling relies on the activity of transmembrane receptors and their presentation on the cellular surface. Their continuous insertion in the plasma membrane is balanced by constitutive and activity dependent internalization, which is orchestrated by adaptor proteins recognizing semi-specific motifs within the receptors' intracellular regions. Here we describe a complementary and evolutionary conserved and refined trafficking mechanism for G-protein coupled receptors (GPCR). This mechanism relies on the insertion of their amphipathic helix 8 into the inner leaflet of lipid membranes, orthogonal to the transmembrane helices. These amphipathic helices dictate subcellular localization of the receptors and autonomously drive their endocytosis by cooperative assembly and association with areas of high membrane curvature. The strength of helix 8 membrane insertion propensity quantitatively predicts the rate of constitutive internalization of GPCRs. This discovery advances our understanding of membrane protein trafficking and highlights a new principle of receptor-lipid interactions that may have broader implications for cellular signaling and therapeutic targeting.

INTRODUCTION

Cellular trafficking and sorting processes direct transmembrane proteins (TMPs) to their proper destination within the cell. Consequently, these processes are of fundamental importance for cellular homeostasis, metabolism, and communication. Malfunction results in diseases including cancer, metabolic syndromes, neuropathies, neuro-degenerative disease and psychiatric disorders [1].

The transport of TMPs between different cellular compartments is mediated through the action of vesicular membrane carriers. Specificity in trafficking itineraries is achieved by selective TMP cargo sorting into these carriers, eventually giving rise to differential localizations of TMPs within the cell. This sorting relies partly on semi-specific protein-protein interactions between compartment specific adaptor proteins (e.g. AP1-5 and GGAs) and short linear motifs within the cargo TMPs (e.g. FXNPXY, tyrosine- and dileucine-based signals) [2,3]. However, these signals are highly ambiguous and offers little predictive power, leaving critical gaps in our understanding of how TMP localization is precisely regulated within cells.

The initial budding and formation of vesicular carriers involves generation of high membrane curvature which serves to recruit specific scaffolding and regulatory cytosolic proteins [4,5]. This mechanism, termed membrane curvature sensing (MCS), is frequently mediated by amphipathic helices (AHs) that insert partially into exposed lipid packing defects in the convex leaflet of curved membranes [6,7]. We hypothesized that AHs in the intracellular termini of TMPs, positioned at the membrane-cytoplasm interface, serve to partition TMPs into areas of high curvature during

39 formation of vesicular carriers thereby serving as a generic mechanism driving differential
40 forward trafficking of TMPs in the endolysosomal system.

41 Using G protein-coupled receptors (GPCRs) as example, our data demonstrates that AHs direct
42 constitutive trafficking and redistribution of TMPs with rates quantitatively predicted by their
43 membrane insertion propensity (MIP). We demonstrate that this new trafficking mechanism of
44 TMPs, which relies on direct association with highly curved membranes in budding membrane
45 carriers, is fundamentally distinct in terms of kinetics and molecular association from
46 conventional adaptor-based TMP trafficking processes, such as agonist-induced internalization.
47 Moreover, we present data suggesting that MIP of GPCR AHs is conserved across GPCR families
48 and animal species and has been refined during the course of evolution. We refer to this novel
49 mechanism as Trafficking of Transmembrane proteins by Amphipathic Motifs (ToTAM) and
50 propose it as a complementary means of cellular sorting and localization to adaptor-based sorting
51 of TMPs.

52 ## RESULTS

53 ### Amphipathic helices drive constitutive internalization of transmembrane proteins

54 G protein-coupled receptors (GPCRs) constitute the largest family of TMPs in the human genome
55 and include receptors for diverse signaling molecules, such as small molecule neurotransmitters,
56 peptides, glycoproteins, lipids, nucleotides, and ions [8]. They control vital physiological functions
57 and represent targets for roughly a third of FDA approved drugs [9]. GPCRs consist of 7
58 transmembrane α-helices and a commonly amphipathic 8th helix (H8) that can insert into the
59 cytosolic leaflet of the membrane orthogonal to the transmembrane helices (Figure 1A) [10–13].

60 Interactions between H8 and cytosolic adaptor proteins are known to mediate various trafficking
61 processes, particularly agonist-induced endocytosis, but also constitutive internalization [14].

62 To test our hypothesis, that AHs in the intracellular termini of TMPs can drive their forward
63 trafficking in the endolysosomal system, we tested the autonomous function of H8 in endocytosis.
64 We fused peptide sequences harboring H8 (17-18 residues) from a number of well-characterized
65 class A GPCRs (rhodopsin (Rho), β2 adrenergic receptor (β_2), substance P receptor (NK_1), and
66 dopamine D2 receptor (D_2)) to the cytosolic C-terminus of the internalization inert
67 transmembrane interleukin-2 receptor a-subunit (IL-2a), hereafter referred to as Tac (Figure 1A)
68 [15,16]. The addition of AHs increased internalization of Tac as determined by quantitative confocal
69 microscopy of antibody feeding experiments in HEK293 cells (up to 10-fold for Tac-D2) (Figure 1B-
70 C). Disrupting the hydrophobic wedge of the amphipathic helices by introducing negative charges
71 (Figure 1A) abrogated this internalization. We recapitulated these findings in HeLa cells (Figure
72 S1). Alanine substitution of cysteines, previously shown to modify trafficking of GPCRs through
73 acylation [17], did not further affect internalization in this context (Figure S2).

74 After confirming the relative internalization rates with high-throughput quantitative flow
75 cytometry [18] (Figure S3), we showed that five additional H8s with distinct amphipathic nature,
76 i.e., with high hydrophobic moment, also increased Tac internalization (Figure 1D). These were
77 H8 from trace amine receptor 1 and 6 (TA_1 and TA_6), kappa opioid receptor (κ), dopamine D1
78 receptor (D_1) and angiotensin 2 type 1 receptor (AT_1) (biochemical parameters outlined in Figure
79 S4). To consolidate and broaden these findings, we also tested non-GPCR helices. Fusion of a
80 hydrophilic helix from troponin[19] or the hydrophobic helix from citrate[20] did not increase Tac
81 internalization, whereas AHs of several membrane-associated proteins involved in membrane

82 trafficking, including Amphipathic Lipid Packing Sensor (ALPS), Sar1 and Endophilin A1, but not
83 Epsin-1[21,22] facilitated internalization (Figure 1E). Similarly, exogenous AHs, including those from
84 the bee venom Melittin and the bacterial protein SpoVM as well as the artificial AH Hecate,
85 strongly facilitated internalization of Tac. Together these findings demonstrate that AHs, diverse
86 in origin and devoid of known adaptor motifs, autonomously increase endocytosis of a
87 transmembrane protein. We refer to this mechanism as Trafficking of Transmembrane proteins
88 by Amphipathic Motifs (ToTAM).

89 The membrane insertion propensity of AHs quantitatively predicts their effect on TMP
90 internalization

91 To quantify the propensity of individual AHs to associate with positive membrane curvature, we
92 calculated the hydrophobic moment of AHs and adjusted it by their intrinsic helical propensity
93 (see methods)[23]. The resulting value, membrane insertion propensity (MIP), correlated with
94 empirical measures of membrane association strength as determined by liposome binding to
95 peptides on a SPOT array (Figure S5). Furthermore, plotting internalization of the AH-fused Tac-
96 constructs as a function of MIP yielded a remarkably strong correlation irrespective of the origin
97 of the AHs (Figure 1F), demonstrating that AHs drive internalization of TMPs in a predictive
98 manner. In comparison, net charge and hydrophobicity demonstrated much lower predictive
99 power on their own (Figure S6). In absolute terms, AHs increased internalization from a basal
100 level of 20% of Tac over a 30-minute period to a complete (100%) turnover of Tac-AHs for the
101 strongest AHs (Figure S7).

102 ## The amphipathic nature of H8 drives constitutive endocytosis of full length GPCRs

103 To address the endocytic function of H8 in context of full-length receptors, we focused on β_2 and
104 AT_1, which contain H8s with pronounced differences in their autonomous endocytic drive (Figure
105 1F, red and blue, respectively). We made chimeric constructs by interchanging their H8s (Figure
106 1G) and assessed their internalization. In concordance with the autonomous drive of their H8s,
107 AT_1 displayed significantly higher constitutive internalization than β_2, and this pattern was fully
108 reversed by swapping their helices (Figure 1H and S8). Furthermore, the introduction of the
109 synthetic, potent AH Hecate (Figure 1G) gave rise to an even higher internalization rate than that
110 of AT_1 H8, in context of both β_2 and AT_1. In contrast, internalization in presence of agonist was
111 robust for all constructs irrespective of AH (Figure 1H and S8). Further, while constitutive
112 internalization scaled linearly with expression, agonist induced internalization for the H8
113 containing constructs deviated from linearity consistent with saturation of adaptor-based
114 internalization machinery (Figure S8)[24]. This suggests that MIP of H8 drives constitutive, but not
115 agonist-induced, internalization of GPCRs in a mechanistically novel fashion.

116 ## AHs in TMPs regulate their cellular distribution at steady state

117 To assess how AHs might affect the steady state distribution of TMPs we adapted a proximity
118 biotinylation approach. We chose a series of five Tac-AH constructs, spanning from low to high
119 MIP values and fused the small (26.4kDa) biotin ligase BioID2[25] to their C-terminal end (Figure
120 2A). Western blot analysis confirmed expression of proteins of the expected size (62kDa, lower
121 band unglycosylated) and further suggested a reduced glycosylation (>75kDA, Upper band) with
122 increasing MIP (Figure 2B, top). The BioID2-fusion constructs recapitulated ToTAM driven
123 internalization as assessed by quantitative confocal microscopy (Figure 2B, bottom and S9A-B).

124 Following a 24-hour incubation with excess biotin, we performed affinity purification of the
125 biotinylated proteins to assess their differential association with the AH containing BioID2-fusion
126 constructs by quantitative label-free LC-MS² [25]. We identified a total of 2569 unique proteins and
127 grouped them by sub-cellular localization according to a negative matrix factorization (NMF)
128 approach previously applied to proximity biotinylation experiments [26] and evaluated relative
129 enrichment of proteins found in TacAH-BioID2 transfected cells versus mock (pcDNA). Proteins
130 belonging to the endolysosomal pathway were among the most enriched (Figure S9C), validating
131 the proximity labelling strategy. Among the subcellular compartments belonging to the
132 endosomal system only "plasma membrane" exhibited significantly differential enrichment
133 across the BioID2-fusion proteins revealing a strong negative association with increasing MIP
134 values consistent with reduced maturation and increased internalization (Figure 2C). Weaker,
135 non-significant trends were observed for the remaining endolysosomal compartments.

136 Upon analysis of the total variance of the data by principal component analysis, we observed a
137 MIP-dependent distinction of protein labelling intensities by TacAH-BioID2 contructs (Figure 2D).
138 We next asked whether MIP—value was associated with any individual proteins. Linear regression
139 analysis of all identified proteins highlighted a subset of proteins which showed strong positive
140 correlation (R^2 >0.4) with MIP (indicated in light blue). Of note, none of the identified adaptor
141 protein (AP) complex subunits (indicated in green) fulfilled these criteria (Figure 2E). Protein
142 network analysis of the strongly MIP correlated subset revealed several tightly connected clusters
143 annotated as related to translation, ER localization, ER import, COPI/II complex and mitophagy
144 (Figure 2F). Interestingly, plotting all identified core proteins of the COPI and COPII complexes
145 revealed an overall increased abundance with MIP (Figure S9D+E). Together these findings

146 suggest a MIP dependent steady state enrichment of TMP within the early biosynthetic pathway
147 as well as a depletion at the plasma membrane.

148 ToTAM is associated with clathrin

149 Since we found no significant associations between MIP and any classical or putative endocytic
150 adapter proteins, we asked more qualitatively how the Tac-BioID2 constructs differentially
151 labelled established components of the endocytic machinery similar to the analysis for the COPI
152 and COPII complexes. The MIP of the expressed Tac-AHs did not significantly affect the
153 enrichment of actin or dynamin, (Figure 3A) consistent with a low impact of treatment with the
154 actin polymerization inhibitor Latrunculin A, EIPA and Dyngo-4A on internalization of Tac-AHs
155 (Figure S10A-C). In comparison, ATP-depletion resulted in a relative reduction of internalization
156 for all constructs (Figure S10D-F), indicating involvement of energy-dependent processes in
157 ToTAM.
158 Next, we addressed association of the Tac-BioID2 constructs with components of specific
159 endocytic pathways. Key proteins of clathrin-mediated endocytosis (CME)[27], in particular clathrin
160 and EPS15, were enriched for all Tac-AHs (Figure 3B). On the other hand, identified components
161 of the CLIC/GEEC pathway, and caveolae[28,29], were consistently less enriched with increasing MIP
162 of the Tac-AHs. Finally, enrichment of proteins involved in alternative endocytic pathways,
163 including Arf6, Rac1, Endophilin A2, and Flotillins (FLOT1 and FLOT2 [30]), was relatively
164 independent of MIP. Taking into account the reduced surface expression of Tac-BioID2 constructs
165 as a function of MIP (dashed line), we interpret that the AHs likely do not actively drive sorting
166 away from CLIC/GEEC or caveolae, but that AHs potentially sort TMPs toward alternative
167 endocytic pathways involving Arf6, Rac1, Endophilin A2, and Flotillins, in addition to CME.

168 Grouping all identified CME associated proteins according to temporally defined modules [31], we
169 observed no marked increase in association with nucleation and assembly, neck constriction or
170 scission and movement modules, while proteins involved in uncoating as well as endosome fusion
171 were enriched for all AHs (Figure S11A). Notably, proteins of the nucleation and formation module
172 that showed increased abundance, including clathrin and EPS15, represented a group that has
173 been shown to be continuously associated with CME events until uncoating [27]. EPS15 is known to
174 recruit ubiquitinated cargo to endocytic sites [32]. In accordance, we detected minor increases in
175 ubiquitin binding proteins of the ESCRT machinery and E3 ubiquitin ligases [33] (Figure S11B+C), as
176 well as the ubiquitin-receptor SQSTM1 (p62) as the top hit among MIP correlated associations
177 (Figure 2E+F). This suggests an interaction with the ubiquitin machinery, despite no evident
178 ubiquitination of the Tac-AH constructs (Figure 2B). Taken together, ToTAM associates with CME
179 and likely with components of alternative pathways, while seemingly avoiding GLIC/GEEC and
180 caveolae in addition to the downstream ubiquitin machinery.

181 ## ToTAM is temporally uncoupled from classical CME

182 To directly evaluate the trafficking dynamics of Tac-AH constructs and the CME structures they
183 associate with, we turned to pulsed pH (ppH) TIRFM assay [34] using super ecliptic pHluorin (SEP)
184 tagged constructs co-expressed with mCherry-tagged clathrin light chain (CLC) (Figure 3C-F and
185 S12). Corroborating the previous findings, the number of endocytic events increased by almost
186 an order of magnitude with increased MIP of the AHs, approaching the rate of the transferrin
187 receptor (TfR) for the strongest helices (H8 from AT_1, and Hecate) (Figure 3E). Interestingly,
188 exocytosis increased correspondingly, suggesting efficient intracellular sorting to recycling

189 endosomes (Figure S13). CLC fluorescence intensity traces associated with TfR endocytic events
190 (red line showing averaged traces) displayed a typical profile with gradual accumulation until
191 point of scission followed by a rapid decrease after scission (Figure 3F). This distinct profile was
192 gradually lost with increasing MIP of the Tac-AH constructs indicating that scission is temporally
193 uncoupled from classical CME, although some spatial association with CLC was retained for all
194 constructs (red line is above the gray line showing the average level of CLC away from endocytic
195 events). Examination of individual normalized traces displayed a range of CLC recruitment profiles
196 (Figure 3F (Lower) and Figure S14). Principal component analysis revealed a decreasing fraction
197 of traces similar to the typical TfR-associated CLC profile for Tac-AHs with increasing MIP (Figure
198 S15). Conversely, an increased fraction of events displayed accumulation of CLC immediate post
199 scission. In summary, increased MIP directs ToTAM towards bulk association with CME core
200 machinery at the expense of other endocytic machineries, while simultaneously decreasing the
201 temporal synchronization and coordination with clathrin-dynamics.

202 ToTAM involves accelerated endocytic maturation and scission

203 Next, we analyzed the recruitment dynamics of the SEP-Tac-AH constructs themselves prior to
204 scission (Figure 4A). While SEP-TfR accumulated at a steady rate during vesicle formation [35], the
205 AH-linked profiles showed fast and accelerating kinetics with increasing MIP of AHs. Fitting these
206 profiles with a logistic equation indicated an increasingly cooperative clustering mechanism
207 consistent with an auto-nucleating function underlying ToTAM (Figure 4B). To determine if this
208 effect translates into a generalized increase in maturation rate of endocytic structures, we
209 performed Tf-uptake in cells expressing the Tac-AH constructs. This demonstrated a strong and
210 MIP dependent increase in transferrin uptake *in trans* (Figure 4C). Cargo load of individual

211 endocytic events determined from the ppH-TIRFM experiments (pH 5.5 fluorescence at the time
212 of scission) was decreased with increasing MIP of AHs (Figure 4D), whereas quenching rates as
213 result of endosomal acidification increased with MIP of AHs (Figure 4E). Relating the cargo load
214 to the acidification rates as a measure of endosome size (3D volume) further suggests an
215 increased cargo density with increasing MIP of AHs (Figure S16). Taken together, we find that
216 ToTAM is characterized by numerous, fast, small and cooperative endocytic events with the
217 potential to accelerate overall trafficking rates.

218 ToTAM associated with high membrane curvature during endocytosis

219 The temporal uncoupling with canonical endocytic machinery as well as the cooperative, high-
220 density recruitment and the inductive properties of ToTAM collectively point to an underlying
221 autonomous and recursive mechanism, consistent with concurrent membrane curvature sensing
222 and induction, which is a common characteristic of AH association with lipid membranes. We
223 therefore investigated the membrane curvature sensing properties of Hecate (the AH tested with
224 highest MIP) in a buckled membrane system using molecular dynamics simulation. This
225 simulation predicted a curvature sensitive membrane sorting (Figure 5A-B), akin to previous
226 findings for ALPS [36]. To experimentally confirm association with high membrane curvature we
227 incubated Bodipy-Tr labelled giant unilamellar vesicles (GUVs) (red) with Oregon green 488
228 labelled Hecate peptide (green). Consistent with the cooperative clustering observed in the ppH-
229 TIRF experiments, the Hecate peptide occasionally formed bulging microdomains on GUVs in the
230 absence of manipulation indicative of membrane curvature induction (Figure 5C).

231 Next, we pulled tethers from GUVs preincubated with OG488-Hecate to generate a high
232 membrane curvature domain, and indeed observed a significant enrichment of the Hecate
233 peptide on the tether (peptide on tether relative to GUV) (Figure 5D-E). A control peptide with
234 similar charge but reduced helical propensity and MIP of the helix, did not bind to GUVs (Figure
235 S17A+B). Given this *in vitro* evidence, we next tested whether the Tac-AH constructs displayed
236 membrane curvature association at the plasma membrane of cells. To assess the size and
237 curvature of the endocytic budding structures encompassing the cargo prior to scission, we
238 antibody-labelled surface expressed Tac-AHs for 3D-dSTORM imaging and identified protein
239 clusters using DBSCAN analysis (Figure 5F and S18). While the median radius of clusters was 100
240 nm for Tac, consistent with the size of clathrin-coated pits [37] cluster sizes were consistently smaller
241 with increasing MIP of AHs (Figure 5G). We further extracted the number of localizations per
242 cluster, enabling us to plot protein densities of individual budding structures as a function of size.
243 In our previous studies, we have demonstrated and rationalized by modelling the membrane
244 curvature sensing by amphipathic insertion into lipid membrane defects give rise to a log-log
245 linear relationship [6]. Indeed, the averaged cargo densities for the different size bins gradually
246 approached a linear relationship (indicated by the dashed line) with increasing MIP of the AHs
247 (Figure 5H). Moreover, the negative slope, which indicates the degree of membrane curvature
248 sensing nominally increased as a function of the MIP of the AH (Figure 5I)[6]. In summary, we
249 propose that ToTAM mechanistically serves both to localize cargo to endocytic pits as well as to
250 facilitate the membrane curvature induction and possibly scission of these pits to drive
251 endocytosis.

252 ## Mapping of MIP in the C-termini of human GPCRs

253 To characterize the membrane association of C-termini across the full range of Human GPCRs, [35]
254 we developed the liposome binding SPOT assay (Figure S5) into a large-scale chip array format
255 using consecutive 16-mer peptides with a 2AA offset (Figure 6A-B). Reconstruction of binding
256 profiles from individual peptide binding values revealed confined membrane binding regions of
257 different strength as illustrated by the C-terminal regions of rhodopsin, β_2 and AT_1 (Figure 6C).
258 These regions overlap with the H8 region as indicated by their high MIP-values. All receptor
259 profiles are displayed in Figure S19. Averaged membrane binding profiles for each of the GPCR
260 families confirmed this pattern for rhodopsin (disregarding olfactory receptors) as well as for
261 secretin and frizzled families, albeit with membrane binding extending slightly further away from
262 the TM region for the latter. Membrane binding was less pronounced for the remaining families
263 and absent from the glutamate receptor family (Figure 6D). Moreover, these binding profiles are
264 in good agreement with the conservation of amphipathic periodicity in H8 across the GPCR
265 families[38] (Figure S20A). Clustering of binding profiles of C-termini from individual receptors
266 revealed a surprisingly large group of GPCRs (cluster 1) without membrane binding (Figure 6E+F).
267 Several of these receptors are from the glutamate receptor family in agreement with the low
268 average profile of the family (Figure 6D). However, many additional receptors belonging to other
269 families and without any clear evolutionary origin, also show no membrane binding. Notably, this
270 is true for many receptors belonging to the Rhodopsin family (Figure S19+20B). Clusters 2-5
271 showed membrane binding profiles consistent with membrane proximal H8, albeit with different
272 intensities of the binding within each cluster and increasing length and distance from TM7 going
273 from cluster 2 to 5 (Figure 6D-E and Figure S19). Finally, cluster 6 contained a wide range of

274 different membrane binding profiles, which are more distant from TM7 and/or contain multiple
275 membrane binding sites.

276 We did not observe a significant enrichment of individual clusters within GPCR receptor families
277 (Figure S20B), or specific tissues (Figure S20C). However, functional enrichment analysis within
278 the studied GPCRs using Gene Ontology (GO) terms revealed a significant enrichment of receptors
279 located to endolysosomal membranes for the bona fide H8 clusters (Clusters 2-5), while non-
280 binding receptors (Cluster 1) are associated with disc-like membranes or membranes with
281 topologies that restrict membrane insertion (Photoreceptor discs and exosomes, respectively)
282 (Figure S21A). Cluster 6 receptors showed a weak association with caveola and growth cones,
283 although driven by a relatively low number of proteins. A wide range of both Molecular Function
284 and Biological Process (BP) terms were associated with all clusters (Figure S21B+C), leading us to
285 perform a semantic similarity GO term enrichment analysis of the significant BP terms (Figure
286 S21D). Consistent with the enrichment of Cluster 1 in Photoreceptor discs, we see a strong
287 association with light related BP terms. Clusters 2-5 show the strongest association with synaptic
288 transmission, particularly driven by receptors with membrane proximal H8 (cluster 2), while the
289 longer and more distal H8 of cluster 5 associates with cellular differentiation processes. Finally,
290 we find that receptors of cluster 6 associate with terms related to peripheral, cardiovascular
291 regulation (Figure S21D).

292 MIP of H8's predicts constitutive internalization of human GPCRs

293 The experimentally derived membrane binding profiles enabled us to delineate bona fide
294 membrane binding H8s (cluster 2-5) and calculate MIP values for these regions (Figure S22). We

295 previously characterized the constitutive internalization of a range of pharmacologically relevant
296 GPCRs [39] and here asked if this internalization could be explained by MIP values of the regions
297 defined by their membrane binding profiles. Indeed, constitutive internalization significantly
298 correlated with MIP values (cluster 2-5) (Figure 6G), demonstrating that the amphipathic nature
299 of H8 can quantitatively predict constitutive endocytosis of full length GPCRs. Other biophysical
300 measures, alternative to MIP, failed to explain constitutive internalization (Figure S23A-C).
301 Consistent with the lack of effects of H8 substitution on agonist induced internalization (Figure
302 1H), MIP did not correlate with agonist-induced internalization (Figure S23D). The complex
303 membrane binding profiles cluster 6 precluded extraction of MIP values predictive of constitutive
304 internalization (Figure S23E). MIP is not significantly related to β-arrestin recruitment or reported
305 G-protein coupling (Figure S24B+C). Together, these results indicate that the MIP of H8 selectively
306 predicts constitutive internalization across this functionally important and structurally well-
307 characterized subset of GPCRs.

308 Given the functional importance of constitutive internalization for dynamic surface expression of
309 GPCRs, we utilized MIP of H8 as a proxy to map predicted internalization rates across all non-
310 odorant GPCRs belonging to cluster 2-5 (Figure 6H and S23F). High MIP values are predominantly
311 observed as phylogenetically related clusters within the rhodopsin family of receptors, including
312 receptors for biogenic amines, chemokine receptors, and MAS-related receptors as well as free
313 fatty acid receptors, alongside individual receptors such as NPBW2 and C5AR1. We also note that
314 Secretin and Frizzled receptors largely contained a H8 predicted or found to be longer than 20
315 residues and the functional significance of this remains to be explored. MIP in GPCRs associated
316 with Fast Endophilin-Mediated Endocytosis (FEME), that mediate endosomal signaling or function

317 as mechanosensors display H8 MIP value distributions that do not deviate significantly from
318 average H8 MIP for all GPCRs (cluster 2-5). On the other hand, GPCRs associated with primary
319 cilia, which exhibit topologies with an inverse curvature to endocytic structures, display H8
320 sequences with significantly lower MIP (Figure S24A). Conversely, GPCRs expressed by viruses,
321 which are known to elicit high constitutive internalization [40], mostly have high MIP values of their
322 H8.

323 ## Membrane insertion propensity is evolutionary conserved across distant organisms

324 To assess potential functional conservation of high MIP of H8, we used available data from UK
325 biobank on naturally occurring variants in human GPCRs. While the cost of individual amino acid
326 substitutions was similar in the H8 region compared to the remaining part of the C-termini (Figure
327 7A), the frequency of non-synonymous natural variants was significantly lower within H8s (Figure
328 7B). When analyzing differences in MIP resulting from these naturally occurring variants, we
329 found that the observed substitutions give rise to a more conserved MIP than substitutions not
330 observed (Figure 7C). Finally, the frequency of natural variants within H8 for individual receptors
331 declines with increasing MIP, emphasizing the functional conservation of high MIP (Figure 7D).

332 Finally, we assessed the evolutionary origin and refinement of MIP in H8 of GPCRs. Using the
333 membrane binding array, we found that GPCR C-termini from evolutionary distant organisms,
334 including C. elegans, D. Melanogaster and S. Cerevisiae, show membrane binding profiles akin to
335 H8 in human GPCRs (cluster 2 and 3) as well as non-binding (cluster 1) and more complex binding
336 profiles (cluster 4 and 5) (Figure 7E and S25). This enabled us to address evolutionary refinement
337 by aligning H8 sequences, as defined in human, across species back to Ecdysozoa (Figure 7F).

338 Individual receptors generally show strong conservation of MIP throughout evolution as indicated
339 by the overall preservation of MIP ranking from yellow to purple across species. The relative
340 variation across species is lowest for H8s with high MIP indicating evolutionary conservation of
341 this feature of H8 (Figure 7F, top). Next, we assessed the distribution of MIP values for individual
342 species across evolution (Figure 7F, histograms to the right). Intriguingly, in ecdysozoa the
343 distribution of MIP values displays a single peak overlaying with values obtained from randomly
344 generated sequences (indicated by the dashed line). However, the fraction of receptors with high
345 MIP of H8 (> 0.3) gradually increases in higher organisms indicating functional significance (Figure
346 7F). This functional selection and refinement are evident from the multimodal distribution of H8
347 MIP values across human GPCRs, significantly different from a normal distribution (Figure 4H, p
348 <0.0001, Shapiro- Wilk). Together, these findings demonstrate both evolutionary selection and
349 refinement as well as functional conservation of the MIP value of H8 in GPCRs.

350 Discussion

351 Here we show that AHs facilitate TMP association with areas of high membrane curvature similar
352 to what has been demonstrated for cytosolic proteins. For TMPs, this association accelerates their
353 constitutive trafficking in a manner that correlates with the MIP of their AHs. While this paper
354 focused on endocytosis, we show evidence that this mechanism, due to the basic biophysical
355 principle, is likely to apply to trafficking events throughout the endomembrane system involving
356 highly curved membrane topologies and serve as a key determinant for steady-state distribution
357 of GPCRs. We term this mechanism ToTAM.

358 Mechanistically, ToTAM is characterized by fast, cooperative cargo recruitment into small,
359 spherical, high-density carriers and thus ToTAM displays elements of both membrane curvature
360 sensing and facilitation of the cargo/carrier complex formation. In fact, ToTAM increases
361 endocytosis of the transferrin receptor in trans, implying an active impact on endocytic processes.
362 During this process, partial biochemical association with CME was observed, however, actual CLC
363 accumulation prior to scission was low and increasingly asynchronous with higher MIP of the AHs.
364 Together, our data suggest that ToTAM might hijack nucleation involving CLC and EPS15 to
365 shortcut classical CME in an autonomous fashion that is complementary to the established
366 adaptor based endocytic machinery.

367 The impact of high MIP H8 specifically on constitutive, and not agonist-induced, internalization of
368 full length GPCRs, was causally demonstrated by experiments with chimeric receptors. Using
369 large-scale liposome-binding data to exclude GPCRs with C-termini that did not display
370 membrane-binding or complex membrane binding enabled us to correlate H8 MIP with full-
371 length constitutive internalization across all human GPCRs. Highest constitutive internalization
372 was predicted for the groups of chemokine receptors, biogenic amine receptors, MAS-related
373 receptors, and free fatty acid receptors. It will be interesting to elucidate the functional
374 implication of the predicted high constitutive turnover with e.g. ligand scavenging, membrane
375 modulating ligands or continuous receptor availability.

376 Another recently described membrane-associated function of H8 is its role in conferring
377 mechanosensitivity to GPCRs [41]. Several of these receptors include a H8 with high MIP, including
378 H_1, AT_1, and $S1P_1$. A putative interplay between mechanosensation and high constitutive
379 internalization due to membrane curvature sensing might reflect two aspects of the same

380 biophysical principle and functional implications of these might unveil themselves perhaps in the
381 context of the cardiovascular system. Moreover, GPCRs implicated in viral entry, as well as virally
382 expressed GPCRs displaying high constitutive internalization, all except mGluR2 show high MIP [42],
383 potentially advocating a novel molecular target for anti-viral therapy. Finally, the simple molecular
384 nature of ToTAM is compatible with an early evolutionary origin, dating back prior to the yeast
385 GPCRs characterized here, conceivably even prior to adaptor based trafficking. Ultimately,
386 functional studies will be needed to settle the evolutionary relation between these two
387 complementary trafficking mechanisms.

388 # References

389 1. McMahon, H. T. & Boucrot, E. Molecular mechanism and physiological functions of clathrin-
390 mediated endocytosis. *Nature Reviews Molecular Cell Biology* vol. 12 517–533 Preprint at
391 https://doi.org/10.1038/nrm3151 (2011).

392 2. Bonifacino, J. S. & Traub, L. M. Signals for sorting of transmembrane proteins to endosomes and
393 lysosomes. *Annual Review of Biochemistry* vol. 72 395–447 Preprint at
394 https://doi.org/10.1146/annurev.biochem.72.121801.161800 (2003).

395 3. Sanger, A., Hirst, J., Davies, A. K. & Robinson, M. S. Adaptor protein complexes and disease at a
396 glance. *J Cell Sci* **132**, (2019).

397 4. McMahon, H. T. & Boucrot, E. Membrane curvature at a glance. *J Cell Sci* **128**, 1065–1070 (2015).

398 5. Antonny, B. Mechanisms of Membrane Curvature Sensing. *Annu Rev Biochem* **80**, 101–123
399 (2011).

400 6. Hatzakis, N. S. *et al.* How curved membranes recruit amphipathic helices and protein anchoring
401 motifs. *Nat Chem Biol* **5**, 835–841 (2009).

402 7. Drin, G. & Antonny, B. Amphipathic helices and membrane curvature. *FEBS Lett* **584**, 1840–1847
403 (2010).

404 8. Bockaert, J. & Pin, J. P. Molecular tinkering of G protein-coupled receptors: An evolutionary
405 success. *EMBO Journal* vol. 18 1723–1729 Preprint at https://doi.org/10.1093/emboj/18.7.1723
406 (1999).

407 9. Hauser, A. S., Attwood, M. M., Rask-Andersen, M., Schiöth, H. B. & Gloriam, D. E. Trends in GPCR
408 drug discovery: New agents, targets and indications. *Nat Rev Drug Discov* **16**, 829–842 (2017).

10. Palczewski, K. *et al.* Crystal Structure of Rhodopsin : A G Protein – Coupled Receptor. **289**, 739–746 (2000).

11. Isberg, V. *et al.* GPCRdb: An information system for G protein-coupled receptors. *Nucleic Acids Res* **44**, D356–D364 (2016).

12. Rosenbaum, D. M., Rasmussen, S. G. F. & Kobilka, B. K. The structure and function of G-protein-coupled receptors. *Nature* vol. 459 356–363 Preprint at https://doi.org/10.1038/nature08144 (2009).

13. Zhang, H. *et al.* Structure of the Angiotensin Receptor Revealed by Serial Femtosecond Crystallography Article Structure of the Angiotensin Receptor Revealed by Serial Femtosecond Crystallography. 833–844 (2015) doi:10.1016/j.cell.2015.04.011.

14. Huynh, J., Thomas, W. G., Aguilar, M. I. & Pattenden, L. K. Role of helix 8 in G protein-coupled receptors based on structure-function studies on the type 1 angiotensin receptor. *Mol Cell Endocrinol* **302**, 118–127 (2009).

15. Bonifacino, J. S., Cosson, P. & Klausner, R. D. Colocalized transmembrane determinants for ER degradation and subunit assembly explain the intracellular fate of TCR chains. *Cell* (1990) doi:10.1016/0092-8674(90)90447-M.

16. Tan, P. K., Waites, C., Liu, Y., Krantz, D. E. & Edwards, R. H. A leucine-based motif mediates the endocytosis of vesicular monoamine and acetylcholine transporters. *Journal of Biological Chemistry* (1998) doi:10.1074/jbc.273.28.17351.

17. Neve, K. A., Qanbar, R. & Bouvier, M. Role of palmitoylation/depalmitoylation reactions in G-protein-coupled receptor function. *Pharmacology and Therapeutics* vol. 97 1–33 Preprint at https://doi.org/10.1016/S0163-7258(02)00300-5 (2003).

18. Mostafapour, S., Kobilka, B. K. & von Zastrow, M. Pharmacological sequestration of a chimeric beta 3/beta 2 adrenergic receptor occurs without a corresponding amount of receptor internalization. *Recept Signal Transduct* **6**, 151–163 (1996).

19. Heidorn, D. B. & Trewhell, J. Comparison of the Crystal and Solution Structures of Calmodulin and Troponin C. *Biochemistry* **27**, 909–915 (1988).

20. Introduction to Protein Structure, by Branden, 2nd Edition: Carl Branden,John Tooze: 9788153230505: Amazon.com: Books. https://www.amazon.com/Introduction-Protein-Structure-Branden-2nd/dp/8153230506.

21. Magdeleine, M. *et al.* A filter at the entrance of the Golgi that selects vesicles according to size and bulk lipid composition. *Elife* (2016) doi:10.7554/eLife.16988.

22. Mesmin, B. *et al.* Two lipid-packing sensor motifs contribute to the sensitivity of ArfGAP1 to membrane curvature. *Biochemistry* **46**, 1779–1790 (2007).

23. Høie, M. H. *et al.* NetSurfP-3.0: accurate and fast prediction of protein structural features by protein language models and deep learning. *Nucleic Acids Res* **50**, W510–W515 (2022).

24. Warren, R. A., Green, F. A., Stenberg, P. E. & Enns, C. A. Distinct Saturable Pathways for the Endocytosis of Different Tyrosine Motifs. *Journal of Biological Chemistry* **273**, 17056–17063 (1998).

25. Kim, D. I. *et al.* An improved smaller biotin ligase for BioID proximity labeling. *Mol Biol Cell* **27**, 1188–1196 (2016).

26. Go, C. D. *et al.* A proximity-dependent biotinylation map of a human cell. *Nature* **595**, 120–124 (2021).

27. Kaksonen, M. & Roux, A. Mechanisms of clathrin-mediated endocytosis. *Nat Rev Mol Cell Biol* **19**, 313–326 (2018).

28. Shafaq-Zadah, M., Dransart, E. & Johannes, L. Clathrin-independent endocytosis, retrograde trafficking, and cell polarity. *Current Opinion in Cell Biology* vol. 65 112–121 Preprint at https://doi.org/10.1016/j.ceb.2020.05.009 (2020).

29. Parton, R. G. Caveolae: Structure, Function, and Relationship to Disease. *Annu Rev Cell Dev Biol* **34**, 111–136 (2018).

30. Casamento, A. & Boucrot, E. Molecular mechanism of Fast Endophilin-Mediated Endocytosis. *Biochemical Journal* vol. 477 2327–2345 Preprint at https://doi.org/10.1042/BCJ20190342 (2020).

31. Traub, L. M. Regarding the Amazing Choreography of Clathrin Coats. *PLoS Biol* **9**, e1001037 (2011).

32. Polo, S. *et al.* A single motif responsible for ubiquitin recognition and monoubiquitination in endocytic proteins. *Nature* **416**, 451–455 (2002).

33. Christ, L., Raiborg, C., Wenzel, E. M., Campsteijn, C. & Stenmark, H. Cellular Functions and Molecular Mechanisms of the ESCRT Membrane-Scission Machinery. *Trends in Biochemical Sciences* vol. 42 42–56 Preprint at https://doi.org/10.1016/j.tibs.2016.08.016 (2017).

34. Merrifield, C. J., Perrais, D. & Zenisek, D. Coupling between clathrin-coated-pit invagination, cortactin recruitment, and membrane scission observed in live cells. *Cell* **121**, 593–606 (2005).

35. Taylor, M. J., Perrais, D. & Merrifield, C. J. A High Precision Survey of the Molecular Dynamics of Mammalian Clathrin-Mediated Endocytosis. *PLoS Biol* **9**, e1000604 (2011).

36. Stroh, K. S. & Risselada, H. J. Quantifying Membrane Curvature Sensing of Peripheral Proteins by Simulated Buckling and Umbrella Sampling. *J Chem Theory Comput* **17**, 5276–5286 (2021).

37. Heuser, J. & Evans, L. Three-dimensional visualization of coated vesicle formation in fibroblasts. *Journal of Cell Biology* **84**, 560–583 (1980).

38. Dijkman, P. M. *et al.* Conformational dynamics of a G protein–coupled receptor helix 8 in lipid membranes. *Sci Adv* **6**, (2020).

39. Schmidt, J. H. *et al.* Constitutive internalization across therapeutically targeted GPCRs correlates with constitutive activity. *Basic Clin Pharmacol Toxicol* **126**, 116–121 (2020).

481 40. Rosenkilde, M. M., Tsutsumi, N., Knerr, J. M., Kildedal, D. F. & Garcia, K. C. Viral G Protein–Coupled
482 Receptors Encoded by β- and γ-Herpesviruses. *https://doi.org/10.1146/annurev-virology-100220-*
483 *113942* **9**, 329–351 (2022).

484 41. Erdogmus, S. *et al.* Helix 8 is the essential structural motif of mechanosensitive GPCRs. *Nat*
485 *Commun* **10**, 1–15 (2019).

486 42. Wang, G. *et al.* The G Protein-Coupled Receptor FFAR2 Promotes Internalization during Influenza
487 A Virus Entry. *J Virol* **94**, (2020).

488 43. Gautier, R., Douguet, D., Antonny, B. & Drin, G. HELIQUEST: a web server to screen sequences
489 with specific -helical properties. *Bioinformatics* **24**, 2101–2102 (2008).

490 44. Jumper, J. *et al.* Highly accurate protein structure prediction with AlphaFold. *Nature* **596**, 583–589
491 (2021).

492 45. Chang, K. T., Guo, J., Di Ronza, A. & Sardiello, M. Aminode: Identification of Evolutionary
493 Constraints in the Human Proteome. *Sci Rep* **8**, 1–8 (2018).

494 46. Sudlow, C. *et al.* UK Biobank: An Open Access Resource for Identifying the Causes of a Wide
495 Range of Complex Diseases of Middle and Old Age. *PLoS Med* **12**, e1001779 (2015).

496 47. Bateman, A. UniProt: A worldwide hub of protein knowledge. *Nucleic Acids Res* **47**, D506–D515
497 (2019).

498 48. Kroeze, W. K. *et al.* PRESTO-Tango as an open-source resource for interrogation of the druggable
499 human GPCRome. *Nat Struct Mol Biol* **22**, 362–369 (2015).

500 49. Hauser, A. S. *et al.* Common coupling map advances GPCR-G protein selectivity. *Elife* **11**, (2022).

501 50. Li, M. Z. & Elledge, S. J. SLIC: A method for sequence- and ligation-independent cloning. *Methods*
502 *in Molecular Biology* **852**, 51–59 (2012).

503 51. Rueden, C. T. *et al.* ImageJ2: ImageJ for the next generation of scientific image data. *BMC*
504 *Bioinformatics* **18**, 529 (2017).

505 52. PedregosaFabian *et al.* Scikit-learn: Machine Learning in Python. *The Journal of Machine Learning*
506 *Research* (2011) doi:10.5555/1953048.2078195.

507 53. Maric, H. M. *et al.* Gephyrin-binding peptides visualize postsynaptic sites and modulate
508 neurotransmission. *Nat Chem Biol* **13**, 153–160 (2017).

509 54. Christensen, N. R. *et al.* Bidirectional protein–protein interactions control liquid–liquid phase
510 separation of PSD-95 and its interaction partners. *iScience* **25**, (2022).

511 55. Hansen, L. B., Buus, S. & Schafer-Nielsen, C. Identification and Mapping of Linear Antibody
512 Epitopes in Human Serum Albumin Using High-Density Peptide Arrays. *PLoS One* **8**, e68902
513 (2013).

514 56. Baddeley, D., Cannell, M. B. & Soeller, C. Three-dimensional sub-100 nm super-resolution imaging
515 of biological samples using a phase ramp in the objective pupil. *Nano Res* **4**, 589–598 (2011).

516 57. Babcock, H., Sigal, Y. M. & Zhuang, X. A high-density 3D localization algorithm for stochastic
517 optical reconstruction microscopy. *Opt Nanoscopy* **1**, 1–10 (2012).

518 58. Tyanova, S., Temu, T. & Cox, J. The MaxQuant computational platform for mass spectrometry-
519 based shotgun proteomics. *Nat Protoc* **11**, 2301–2319 (2016).

520 59. Weinberger, A. *et al.* Gel-assisted formation of giant unilamellar vesicles. *Biophys J* **105**, 154–164
521 (2013).

522 60. Prévost, C., Tsai, F. C., Bassereau, P. & Simunovic, M. Pulling membrane nanotubes from giant
523 unilamellar vesicles. *Journal of Visualized Experiments* **2017**, (2017).

524

525 Correspondence

526 Correspondence and requests for materials should be addressed to Kenneth Lindegaard Madsen.

527 Email: kennethma@sund.ku.dk

528 Acknowledgments

529 We acknowledge the Proteomics Research Infrastructure, Core Facility for Integrated

530 Microscopy and Flow Cytometry and Single Cell Analysis facilities at the University of

531 Copenhagen. Further, we would like to thank Nabeela Khadim for technical assistance.

532

533 Author contributions

534 Conceptualization: KLM, UG, JHS, RH

535 Methodology: KLM, JHS, RH, NRC, ALE, MDL, JR, AHL, MS, MP, KAA, CKH, JPC, DP, PB, VH, ASH

536 Investigation: KLM, JHS, RH, JR, AHL, MS, MP, KAA, MDL, ALE

537 Visualization: KLM, JHS, RH, JR, AHL, MS, TTEN, DP

538 Funding acquisition: KLM, UG, AHL, PB, DP, VH

539 Project administration: KLM

Supervision: KLM, DP, PB, CKH

Writing – original draft: KLM, JHS, RH

Writing – review & editing: KLM, JHS, RH, JR, FH, AHL

Competing interests

Authors declare that they have no competing interests.

Funding

KLM: Danish Research Counsil (DFF), Medical Sciences, Research project 1 (2034-00395A) and Lundbeckfonden, Lundbeck Foundation Experiment (R324-2019-1806)

AHL: Lundbeck Foundation grant R347-2020-2339,

PB is member of the Labex Cell(n)Scale (ANR-11-LABX0038) and ParisSciences et Lettres (ANR-10-IDEX-0001-02). Her group (FRM EQU202003010307 team) is supported by a grant from the Fondation pour la Recherche Médicale (FRM).

Figures and legends

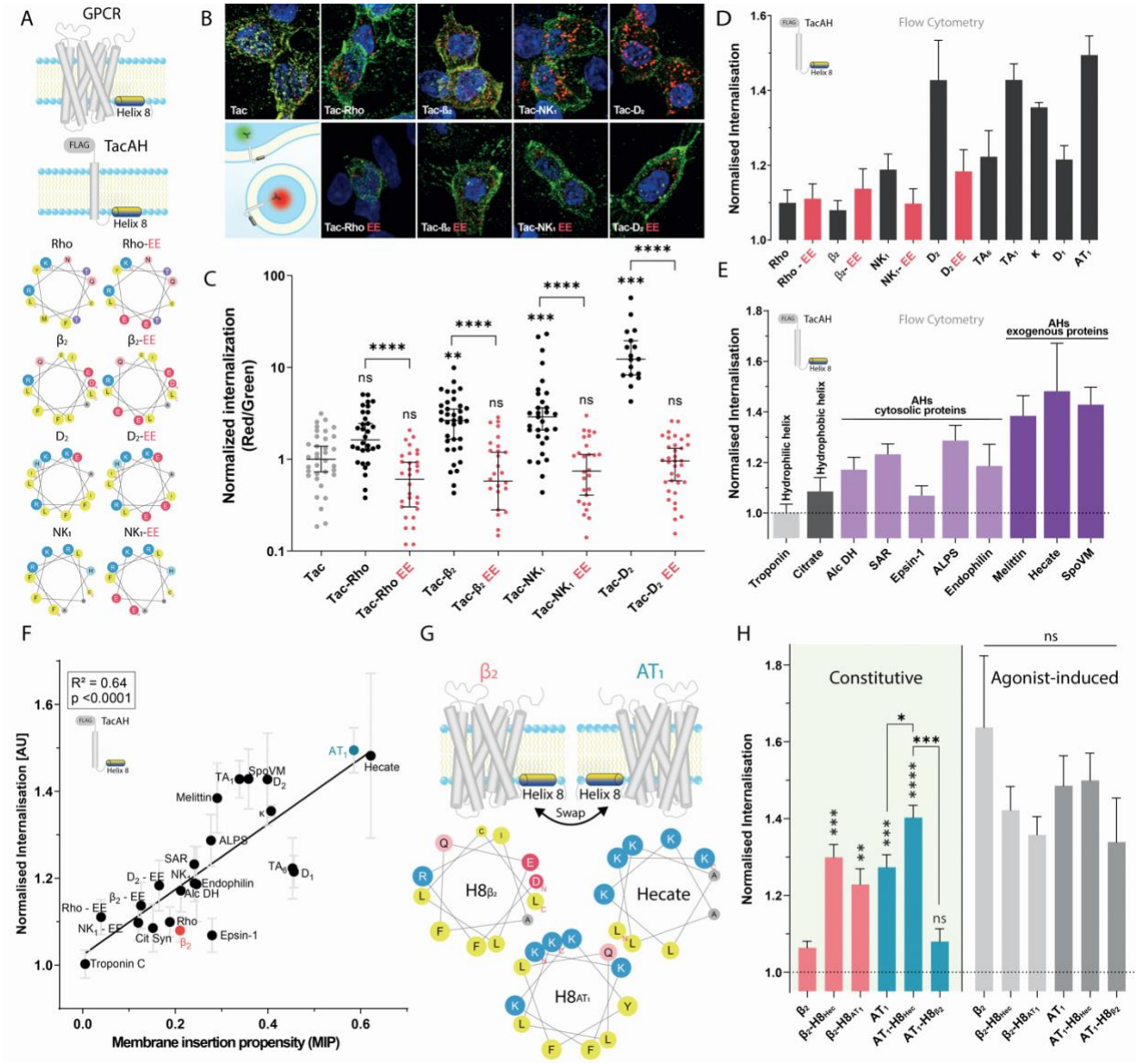

Figure 1. **Amphipathic helices in transmembrane proteins autonomously drive their endocytosis.**

(A) Illustration of GPCR H8 sequences transferred to the single transmembrane protein Tac for determination of their autonomous endocytic drive alongside mutational disruption of amphipathicity by introduction of negative charges in the hydrophobic face of H8.

(B) Representative images of HEK293 cells transfected with Tac-H8 constructs and subjected to antibody feeding (illustrated in insert, lower left).

569 **(C)** Quantification of internalization (Red/Green fluorescence ratio), relative to Tac, from

570 confocal images (every dot represents a cell) N=3.

571 **(D)** Internalization of Tac-H8 constructs assessed by flow cytometry and normalized to Tac.

572 Mean ± SEM, N=3.

573 **(E)** Internalization of Tac with AHs from cytosolic proteins or exogenous AHs assessed by flow

574 cytometry. Mean ± SEM, N=3.

575 **(F)** Linear correlation (R^2 = 0.64 p <0.0001) between Membrane Insertion Propensity (MIP) of

576 Tac-AH constructs and their respective endocytic rate (relative to Tac). Mean ± SEM, N=3.

577 **(G)** Illustration of chimeric H8 GPCRs with swapped part highlighted in helical wheel

578 representations using HeliQuest [43].

579 **(H)** Constitutive and agonist-induced (10 µM agonists; ISO = Isoproterenol and ANGII =

580 angiotensin II) internalization rates of chimeric FLAG-tagged GPCR constructs with swapped H8

581 sequences relative to Tac. Mean ± SEM, N=3.

582

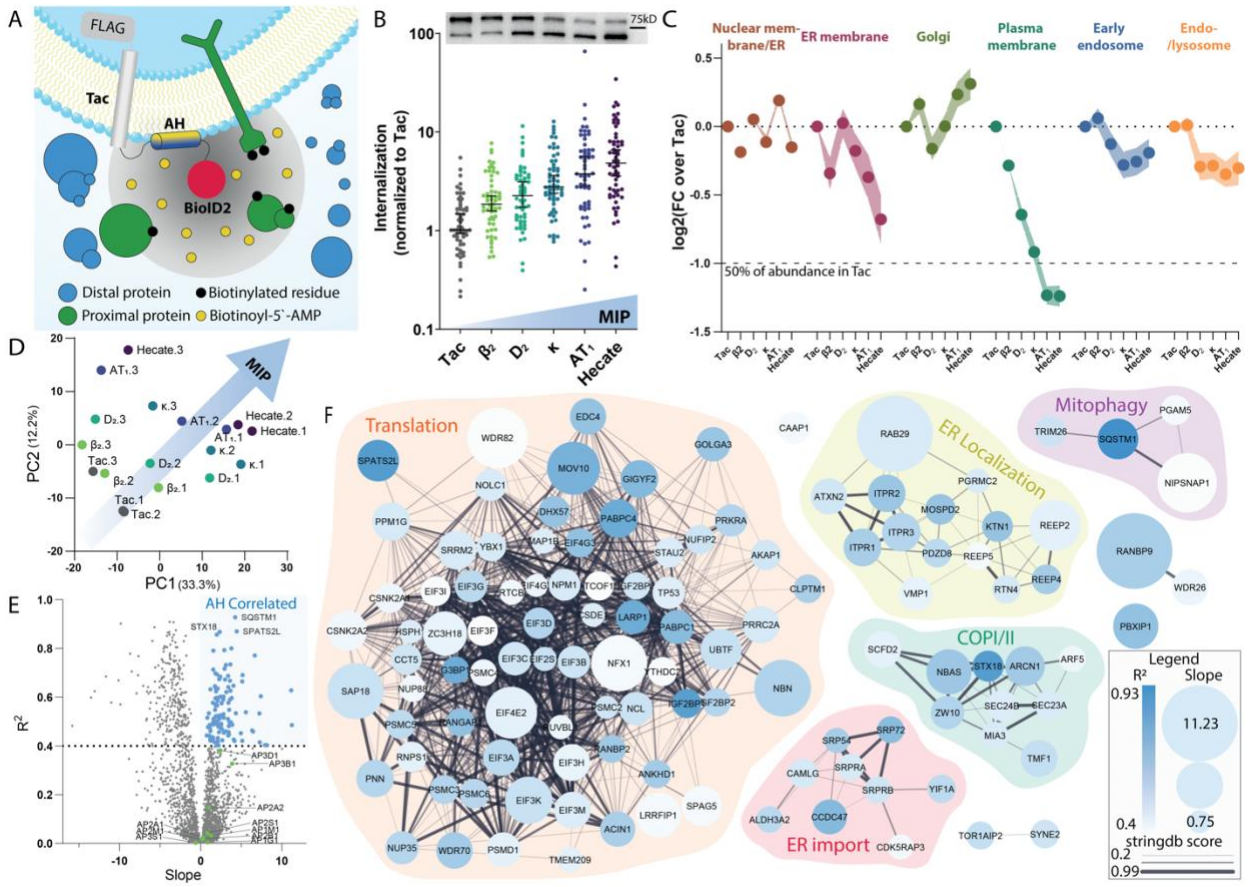

583

584 Figure 2. **Increasing MIP drives association with the biosynthetic pathway and away from the**

585 **plasma membrane.**

586 **(A)** Schematic of proximity biotinylation assay with BioID2.

587 **(B)** (Upper) Western blot (M1 ab) of Flag-Tac AH-BioID2 constructs transfected in HEK293 cells

588 showing mature proteins (high MW band) and immature protein (low MW band). (Lower)

589 Quantification of internalization of Flag-Tac AH BioID2 constructs from confocal images (every

590 dot represents a cell, compiled from three independent experiments).

591 **(C)** Differences in label-free quantification (LFQ) values for indicated constructs versus basal

592 levels (pcDNA) normalized to Tac compiled for all identified proteins belonging to

593 endolysosomal compartments of MMF grouping in [26].

594 **(D)** Principal component analysis biplot showing spread of MS samples along principal

595 component 1 and 2 indicating a MIP driven separation.

596 **(E)** Volcano plot highlighting slope and r^2 values of linear correlations for each identified protein

597 with MIP of the Tac-AH-BioID2 constructs. Protein correlating with MIP (slope > 0 and $r^2 > 0.4$)

598 highlighted in blue. Identified adaptor protein (AP) complex subunits (indicated in green).

599 **(F)** STRING protein network analysis of the proteins identified as MIP correlated in (E) in

600 functional groups based on database annotations.

601

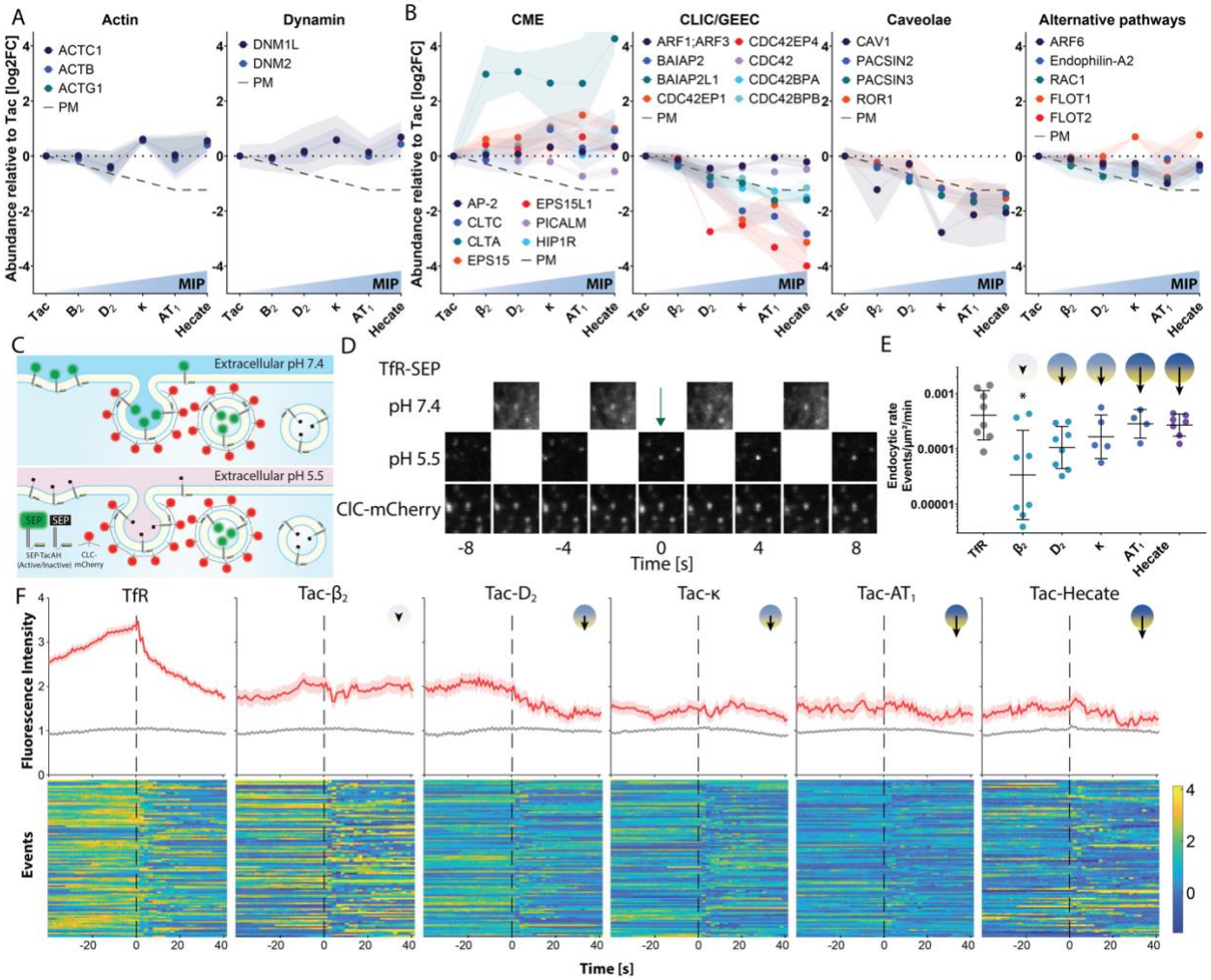

Figure 3. ToTAM associates with CME machinery in a non-canonical manner.

(A+B) Absolute difference in LFQ values (normalized to Tac) of identified actin and dynamin subunits (A) and selected identified proteins associated with CME, CLIG/GEEC, Caveolae and other endocytic pathways (B).

(C) Schematic of (ppH-TIRFM) protocol enabling definition of time of scission for individual endocytic events.

(D) Images of representative endocytic event from ppHTIRFM experiments of Super Ecliptic pHluorin (SEP) tagged transferrin receptor (TfR) together with clathrin light chain (CLC)-mCherry.

612 **(E)** Endocytic event rate for the 5 different SEP-TacAH constructs compared to TfR-SEP. Statistical

613 analysis using Kruskal-Wallis multiple comparisons test.

614 **(F)** (Upper) Average of individually normalized CLC-mCherry traces for TfR-SEP and 5 SEP-TacAH

615 constructs. (Lower) Heatmaps of normalized individual CLC-mCherry traces pre- and post-

616 scission. N = 5-10 cells (846-2797 events) per condition.

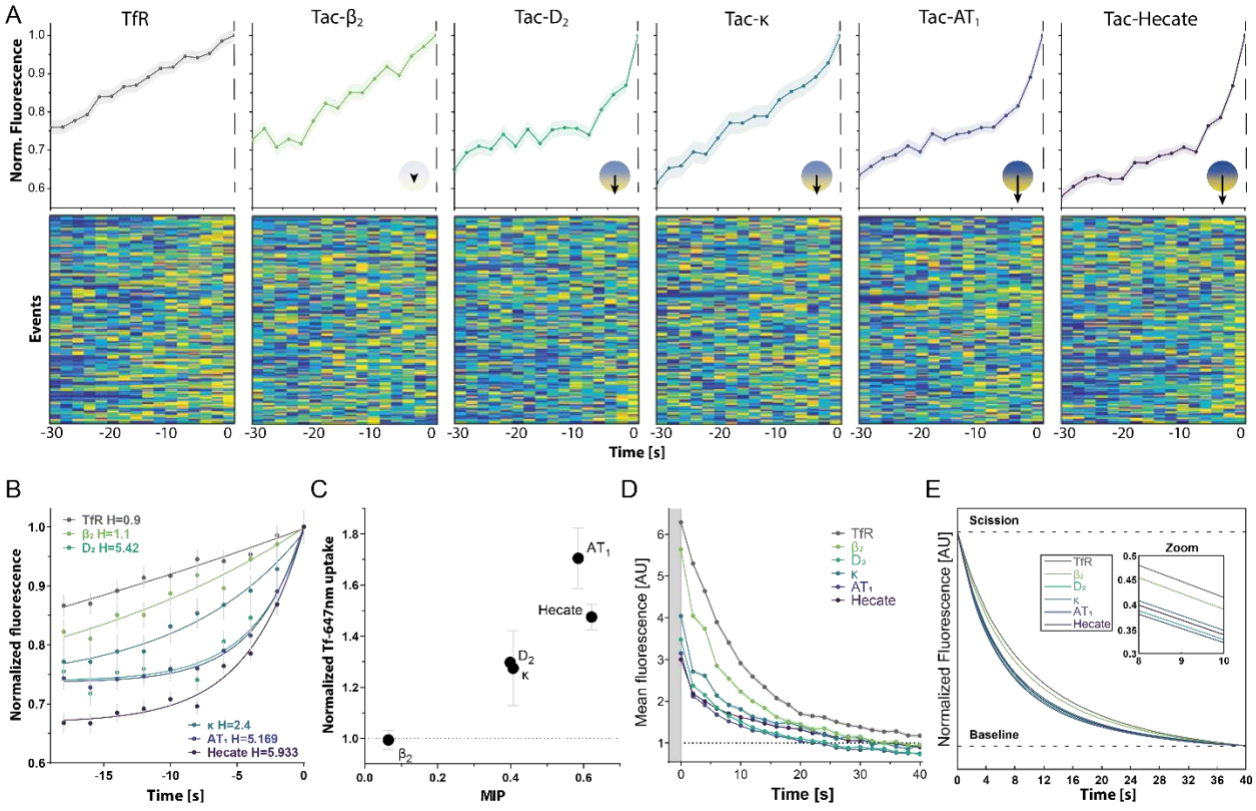

Figure 4. **ToTAM involves accelerated endocytic maturation and scission**

(A) (Upper) Average of individually normalized pH 7.4 TfR-SEP and SEP-TacAH fluorescence intensity traces building up to point of scission (Time = 0). (Lower) Heatmaps of normalized individual SEP-fluorescence profiles at pH 7.4 of TfR-SEP and SEP-TacAH constructs prior to scission. N = 5-10 cells per condition, n = 518-2367 total traces.

(B) Non-linear regression fits of averaged normalized pHluorin traces up to point of scission. H is the Hill coefficient.

(C) Effect of TacAH constructs on AF647-labelled transferrin endocytosis in trans, by flow cytometry.

(D) Averaged fluorescent traces measured at pH 5.5 in cell populations expressing either of the six indicated SEP-TacAH-constructs. Absolute values shown post-scission (t=0).

630 **(E)** Average traces from (D) are normalized to initial fluorescence observed at time of scission

631 (t=0) and fitted to the "Acidification Kinetics Function" (see methods). Fits shown for all six SEP-

632 TacAH-constructs with TfR eliciting slowest acidification kinetics, while AT_1 elicits the fastest

633 acidification kinetics.

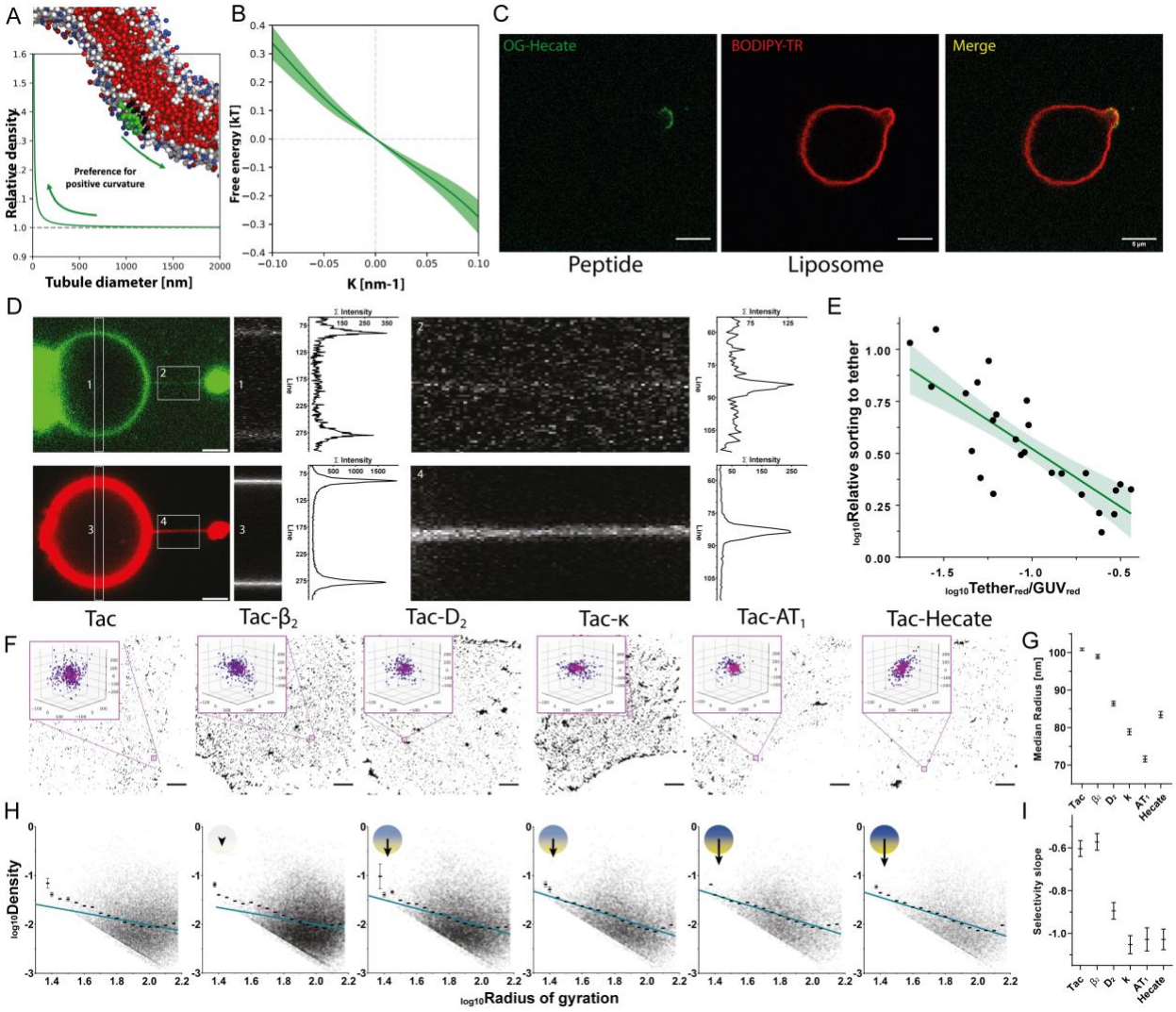

Figure 5. ToTAM involves association with high membrane curvature during endocytosis

(A) Relative protein density (Hecate peptide) as a function of tubule diameter determined in buckled membrane MD analysis indicating a strong preference for positive curvature.

(B) Free energy from (A) as a function of membrane curvature.

(C) Representative images of Oregon Green 488 labeled Hecate (green) bound to free floating BODIPY-TR labeled GUVs (red) revealing selective organization of peptides in deformed microdomain structures on the GUVs. Scale bars indicate 5 µm.

642 **(D)** Tethers pulled from GUVs (red) pre-incubated with Oregon Green labelled Hecate peptide
643 (green). Insert 1 and 3, zooms of GUV and summed intensity profile. Insert 2 and 4, zooms of
644 tether and summed intensity profile.
645 **(E)** Quantification of the relative sorting to the tether as a function of relative size of the tether
646 (Tethered/GUVred).
647 **(F)** Representative 3D-dSTORM images of FLAG-Tac and 5 FLAG-TacAH constructs after surface
648 labelling with Alexa Fluor 647-conjugated M1 α-FLAG antibody, scale bar 5 µm. Inserts show
649 representative single clusters color coded for localization density.
650 **(G)** Average size of clusters for the individual constructs, median $\pm$ 95% CI, N=6.
651 **(H)** Logarithmic relationship of cluster size and cargo density (FLAG-Tac-AH). Black bars show
652 binned averages $\pm$ SEM and the blue line represents a linear fit of the data. Better adherence of
653 the fit to the binned averages indicates curvature dependent sorting for Tac-AH constructs with
654 high MIP.
655 **(I)** Selectivity slope (i.e., curvature sensitivity) derived for linear fits with error on log-log plots of
656 the data in (H) (see Figure S18).
657

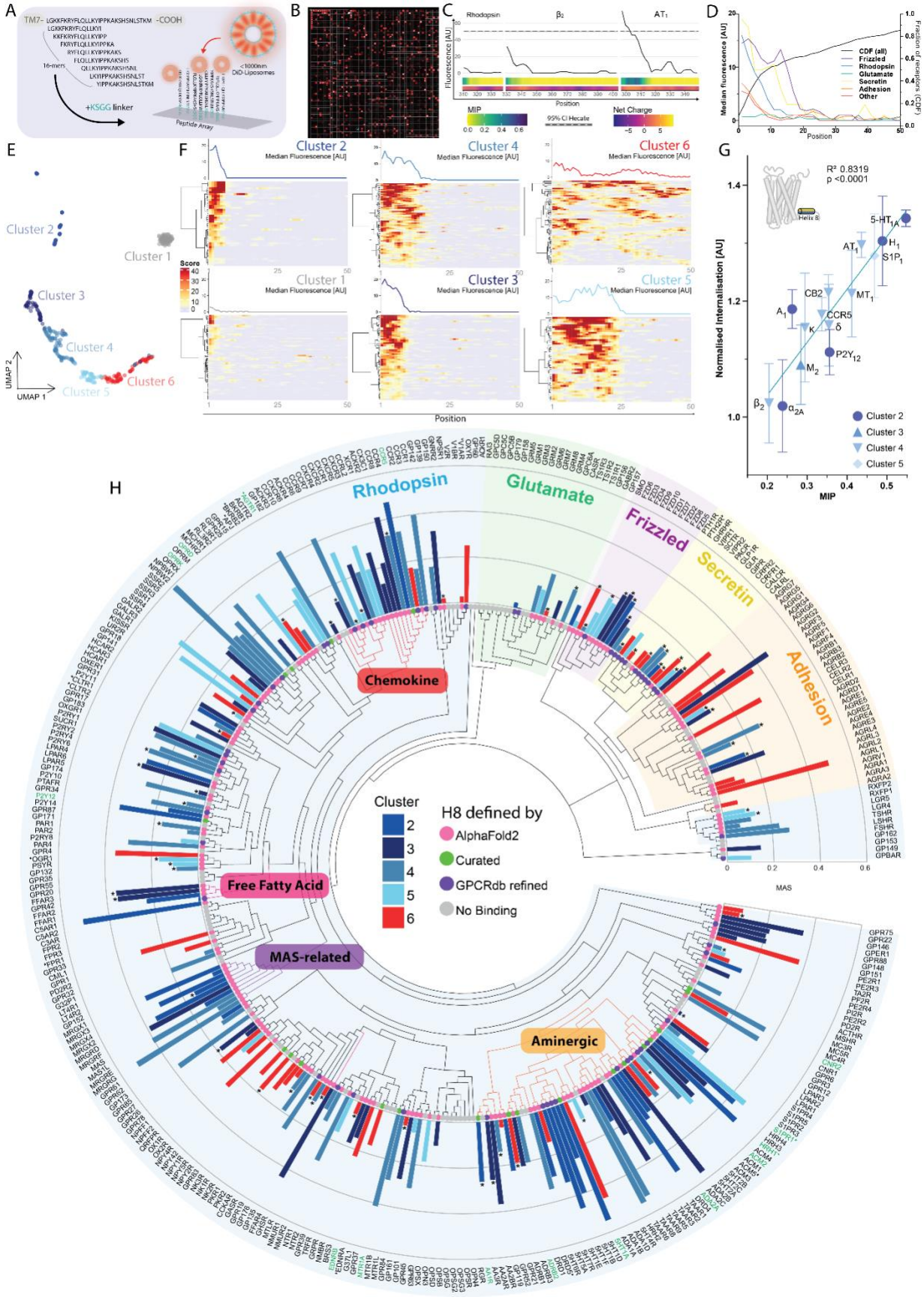
A
TM7- LGKKFKRYFLQLLKYIPPKAKSHSNLSTKM -COOH
16-mers
+KSGG linker
<1000nm DiD Liposomes
Peptide Array
B
C
Rhodopsin
β2
AT1
Fluorescence [AU]
Position
MIP
95% CI Hecate
Net Charge
D
Median fluorescence [AU]
Fraction of receptors (CDF)
CDF (all)
Frizzled
Rhodopsin
Glutamate
Secretin
Adhesion
Other
Position
E
Cluster 1
Cluster 2
Cluster 3
Cluster 4
Cluster 5
Cluster 6
UMAP 1
UMAP 2
F
Cluster 2
Cluster 4
Cluster 6
Cluster 1
Cluster 3
Cluster 5
Median Fluorescence [AU]
Score
Position
G
R² 0.8319
p <0.0001
Helix 8
5-HT1A
H1
S1P1
AT1
CB2
MT1
A1
CCR5
κ
δ
P2Y12
M2
β2
α2A
Normalised Internalisation [AU]
MIP
Cluster 2
Cluster 3
Cluster 4
Cluster 5
H
Rhodopsin
Glutamate
Frizzled
Secretin
Adhesion
Chemokine
Free Fatty Acid
MAS-related
Aminergic
Cluster
2
3
4
5
6
H8 defined by
AlphaFold2
Curated
GPCRdb refined
No Binding
MAS

658

659 Figure 6. **Proteome-wide characterization of C-terminal membrane interactions in GPCRs and**

660 **their role in constitutive endocytosis of GPCRs.**

661 **(A)** Schematic of chip array for scanning of liposome binding strength throughout the full range

662 of human GPCR C-termini at dual AA resolution. Individual peptides are randomly positioned on

663 the chip.

664 **(B)** Representative image of fluorescent signal from bound liposomes on zoomed in area of

665 array. Regular pattern in top left corner is control Hecate peptide.

666 **(C)** Compiled binding profile of the C-termini of Rhodopsin, β_2 and AT_1 along with corresponding

667 MIP and net charge values displayed below.

668 **(D)** Average liposome binding profiles of peptide sequences corresponding to 16 amino acid

669 stretches of GPCR C-termini split by GRAFS family (left y-axis) and cumulative distribution

670 function of all human GPCR C-terminals length (right y-axis) starting at 16 amino acids.

671 **(E)** UMAP-based clustering of all human GPCR C-termini based on position and strength of

672 liposome binding.

673 **(F)** Heatmaps of all individual GPCR C-terminal liposome binding profiles within the six clusters

674 and profile plots of the median fluorescence intensity (line above) (see S20 from detailed view).

675 **(G)** Linear correlation ($R^2 = 0.83$, $p < 0.0001$) between MIP of H8 from clusters 2-5, based on

676 sequences (Figure S22) in most pharmacologically relevant GPCRs and their respective

677 endocytic rate (relative to Tac) determined by flow cytometry [39]. Mean $\pm$ SEM, N=3.

678 **(H)** Circular phylogenetic tree of human GPCRs based on sequence homology and divided into
679 GRAFS families and clusters, alongside the corresponding calculated MIP based on H8 from
680 either refined representative structures as annotated on GPCRdb (purple) [11], AlphaFold2
681 prediction (magenta) [44] or manually curated. Receptors used in (G) are highlighted by green and
682 receptors described as mechanosensitive [41] are highlighted by asterisks (name). GPCRs from
683 cluster 1 (no binding) in grey. Receptors with a structural H8 predicted longer than 20 amino
684 acids marked with asterisk (bar).

685

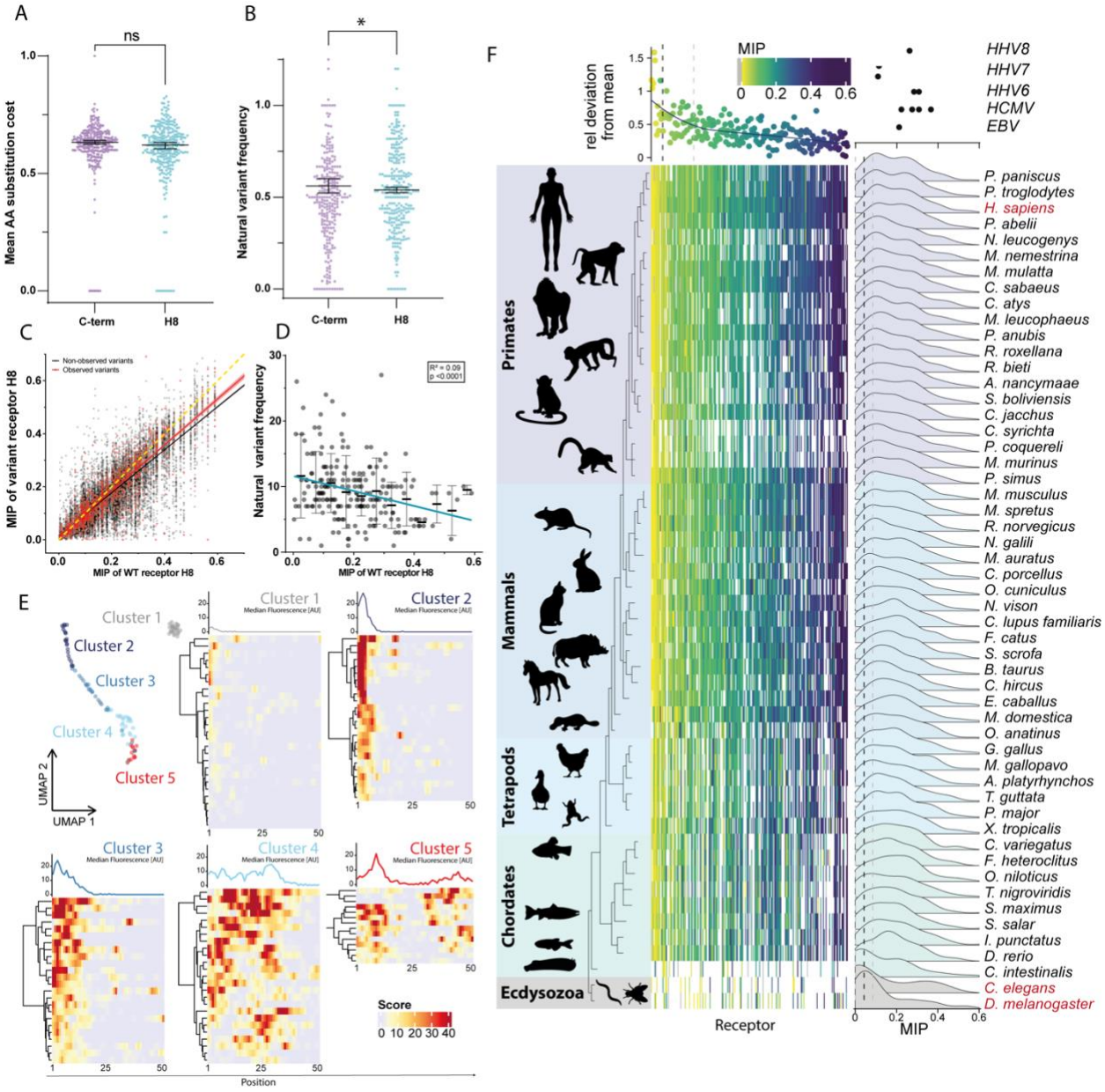

686

687 Figure 7. **Functional conservation and evolutionary refinement of MIP of H8 in GPCRs.**

688 **(A)** Normalised BLOSUM62 [45] substitution cost of natural variants mapped to C-term vs H8.

689 **(B)** Frequency of natural variants in the C-term vs H8 of human GPCRs of clusters 2-6 identified

690 in individuals registered in the UK Biobank [46].

691 **(A and B)** Wilcoxon non-parametric statistical test applied. Asterisks indicate p value <0.05 and

692 ns: p value >0.05.

693 **(C)** Scatter plot of the calculated MIP values of all identified non-synonymous natural variants

694 (red dots) identified in the UK Biobank [46] and non-identified possible non-synonymous

695 substitutions (black dots) as a function of the receptors wildtype MIP. Linear regression analysis

696 of observed natural variants with a slope of 0.87 ±0.01 is closer to full conservation (Indicated

697 by dashed yellow line, slope of 1) than for non-observed 0.81 ±0.004 (all other possible

698 variants). This highlights a relative conservation of MIP.

699 **(D)** Scatter plot showing frequency of non-synonymous natural variants of individual GPCRs as a

700 function of MIP (each receptor represented by a dot), with a negative linear correlation

701 indicating lowered variant frequency for receptors with high MIP (Cyan, $R^2 = 0.089$, $p < 0.0001$).

702 Lines indicate average frequency of binned MIP intervals +/- SD.

703 **(E)** UMAP-based clustering of combined *D. melanogaster*, *C. elegans* and *S. cerevisiae* GPCR C-

704 termini based on position and strength of liposome binding motifs. Heatmaps of individual

705 GPCR C-terminal liposome binding profiles within the 5 clusters and profile plots of their median

706 fluorescence (Top) (See Figure S24 for list of individual receptor and species).

707 **(F)** Evolutionary tree of GPCRs displaying MIP of H8 sequences identified in Human receptors

708 and aligned across species (left). The ratio of variance vs. mean of all MIP decrease with

709 increasing MIP (upper, left). (Upper, right) MIP values for viral GPCRs (Table S2). (Lower right)

710 Density distribution of MIP values for individual species shift to the right during evolution.

711